IOP Publishing Nano Futures 2 (2018) 011001 https://doi.org/10.1088/2399-1984/aab25d

NANO
FUTURES

RECEIVED
2 February 2018

ACCEPTED FOR PUBLICATION
26 February 2018

PUBLISHED
19 March 2018

LETTER

Multimodal hard x-ray imaging with resolution approaching 10 nm for studies in material science

Hanfei Yan[1], Nathalie Bouet[1], Juan Zhou[1], Xiaojing Huang[1], Evgeny Nazaretski[1], Weihe Xu[1], Alex P Cocco[2], Wilson K S Chiu[2], Kyle S Brinkman[3] and Yong S Chu[1]

[1] National Synchrotron Light Source II, Brookhaven National Laboratory, Upton, NY 11973, United States of America
[2] Department of Mechanical Engineering, University of Connecticut, Storrs, CT 06269, United States of America
[3] Department of Materials Science and Engineering, Clemson University, Clemson, SC 29634, United States of America

E-mail: hyan@bnl.gov

Keywords: x-ray nanoscale imaging, high spatial resolution, multimodal imaging, mixed ionic-electronic conducting membrane

Abstract

We report multimodal scanning hard x-ray imaging with spatial resolution approaching 10 nm and its application to contemporary studies in the field of material science. The high spatial resolution is achieved by focusing hard x-rays with two crossed multilayer Laue lenses and raster-scanning a sample with respect to the nanofocusing optics. Various techniques are used to characterize and verify the achieved focus size and imaging resolution. The multimodal imaging is realized by utilizing simultaneously absorption-, phase-, and fluorescence-contrast mechanisms. The combination of high spatial resolution and multimodal imaging enables a comprehensive study of a sample on a very fine length scale. In this work, the unique multimodal imaging capability was used to investigate a mixed ionic-electronic conducting ceramic-based membrane material employed in solid oxide fuel cells and membrane separations (compound of $Ce_{0.8}Gd_{0.2}O_{2-x}$ and $CoFe_2O_4$) which revealed the existence of an emergent material phase and quantified the chemical complexity at the nanoscale.

1. Introduction

Scanning hard x-ray microscopy (SHXM) has undergone rapid development over the last two decades. The emergence of new imaging methods [1, 2] and the advancements in hard x-ray nanofocusing optics [3, 4] have greatly extended the range of SHXM applications, and pushed the achieved spatial resolution to a nanometer scale as well. Multimodal imaging capability offered in the scanning mode engenders a strong demand for SHXM across a wide spectrum of scientific problems. Many nanoprobe beamlines have been or are being constructed at synchrotron facilities over the world [5–10]. In order to achieve high spatial resolution in SHXM, the focusing optic must efficiently focus hard x-rays down to a nanometer scale. Various types of hard x-ray nanofocusing optics have been developed and some of them have demonstrated well-below 20 nm focusing performance [11–13]. However, practical implementation of sub-20 nm hard x-ray scanning imaging still remains challenging because of other requirements. For example, the produced point focus should have a concentrated central peak with low side lobes. Real scientific investigations also require a comfortable working distance, high instrument stability, and sufficient flux in the focus. Recently, Da Silva *et al* reported the achievement of a 12×13 nm^2 nanoprobe at 33.6 keV using Kirkpatrick-Baez mirrors [14]. Here, we report experimental results using multilayer Laue lenses (MLL) [15] to achieve a 13.9×12.3 nm^2 nanoprobe at 12 keV photon energy for scientific investigations. In addition, we show simultaneous multimodal imaging through absorption-, phase- and fluorescence-contrast with equivalent or better spatial resolution.

The goal of this paper is two-fold: firstly, we demonstrate the multimodal imaging with a spatial resolution approaching 10 nm, and confirm it with a variety of characterization methods, secondly we evaluate a model of materials system of interest in material science to fill the current gap between resolution demonstration and real scientific applications.

We characterized the focus size of a pair of crossed MLLs using ptychography reconstruction technique and conventional knife-edge scan, and the imaging resolution of the acquired florescence image using power spectrum density (PSD) analysis. The fitting to knife-edge scan yields a full-width-at-half-maximum (FWHM) focus size of 15.3×16.9 nm^2, while using ptychography reconstruction we obtain a FWHM size of 13.9×12.3 nm^2. PSD analysis of the fluorescence image of a test pattern results in the smallest detectable feature size down to 10.3×10.8 nm^2, determined from the cut-off frequency. We discuss meanings of and differences between these numbers. These independent measurements provide convincing evidence that the achieved imaging resolution approaches 10 nm.

In addition, we demonstrate the effectiveness of multimodal imaging at a nanometer scale by imaging grain boundaries of an ionic-electronic conducting (MIEC) membrane, which has been receiving considerable scientific attention due to their applications in energy conversion and storage including solid oxide fuel cells, and high temperature gas separation membranes [16–22]. The combination of high resolution and multimodal imaging enabled us to view the elemental distribution and structural variations with unprecedented details, and help shed light on the link of new emerging material phase with the membrane's performance. It demonstrates that the advancement in the SHXM enables new imaging capabilities that open up opportunity to tackle diversified scientific problems.

2. Results

2.1. Experiment

The experiment was conducted at the Hard x-ray Nanoprobe Beamline (HXN) of the National Synchrotron Light Source II of the Brookhaven National Laboratory. A coherent and monochromatic beam at 12 keV was delivered to the nanoscale multimodal imaging instrument (nano-Mii) [23] after being conditioned through various beamline optics. A beam-defining aperture in front of the microscope shapes the incidence beam to a rectangle for the nanofocusing optics. Two MLLs, one with a 53 μm lateral aperture and a 4 nm outmost zone width and the other with a 43 μm aperture and a 4 nm outmost zone width, were used to focus x-rays in vertical and horizontal directions (thereafter referred as vMLL and hMLL), respectively. After full optics alignment, the sample positioned in a common focal plane of both vMLL and hMLL lenses was raster-scanned through the nanofocus. An energy-dispersive detector (Vortex, three-element silicon drift detector), which was oriented at 90° with respect to the optical axis, was used to collect fluorescence signals for elemental imaging, and a pixel-array detector (Merlin, 512×512 pixels and a 55 μm pixel size) located 0.5 m downstream was used to capture far-field diffraction patterns of the transmitted nanobeam for absorption and phase imaging. Figure 1 shows schematic drawing of the experimental set up.

Our lens system was designed to produce theoretical diffraction-limited point focus of 10×10 nm^2 size, based on Rayleigh criterion. However, both MLLs contain minor zone placement errors introduced during deposition process [12]. In addition, two MLLs need to be placed in a crossed geometry in order to produce a point focus [24], and a manipulator with eight degrees of freedoms is required to fully align the lenses [25]. Misalignment between two MLLs can also introduce aberration and cause focus broadening [26]. Consequently, the actual focus size is usually slightly larger than the diffraction-limited value.

2.2. Resolution characterization

In order to evaluate the focusing performance, we applied a ptychography technique in which both the complex-valued probe and object functions were reconstructed [2]. In such an experiment, we raster scanned a 2D pattern formed by cubic Au nanoparticles with monodispersive sizes of ~50 nm. Figure 2(a) is the obtained fluorescence image, while figure 2(b) shows the ptychography phase reconstruction of the same area. We want to point out that a fly scan with a square grid of 100×100 points was performed, so that both fluorescence and phase images were obtained simultaneously. Ptychography with fly scan has been demonstrated by many groups before [27–30]. Our recent study shows that the periodic aliasing artifacts often seen in a rectangular grid scan can be mitigated by sufficient overlap between steps [31]. Here we choose 10 nm step to balance the number of scan points and the percentage of overlap, so that the dataset size is not too big to handle and meanwhile the periodic artifacts are negligible. As one can see, the reconstructed phase image gives much better resolution as compared with the fluorescence. Inter-particle gap as small as 10 nm is well resolved in figure 2(b). This indicates that the probe function has been properly deconvoluted from the transmission function. Figure 2(c) depict the reconstructed complex wavefield of the probe in the sample plane (inset) and intensity profiles across the center in two directions. Sharp central peaks with relatively weak side lobes can be seen. A Gaussian fit to the central peak results in a FWHM size of 13.9 nm for the hMLL and 12.3 nm for the vMLL, respectively. Considering minor zone placement error in the lens and other possible broadening effects, these numbers are in good agreement with our predictions.

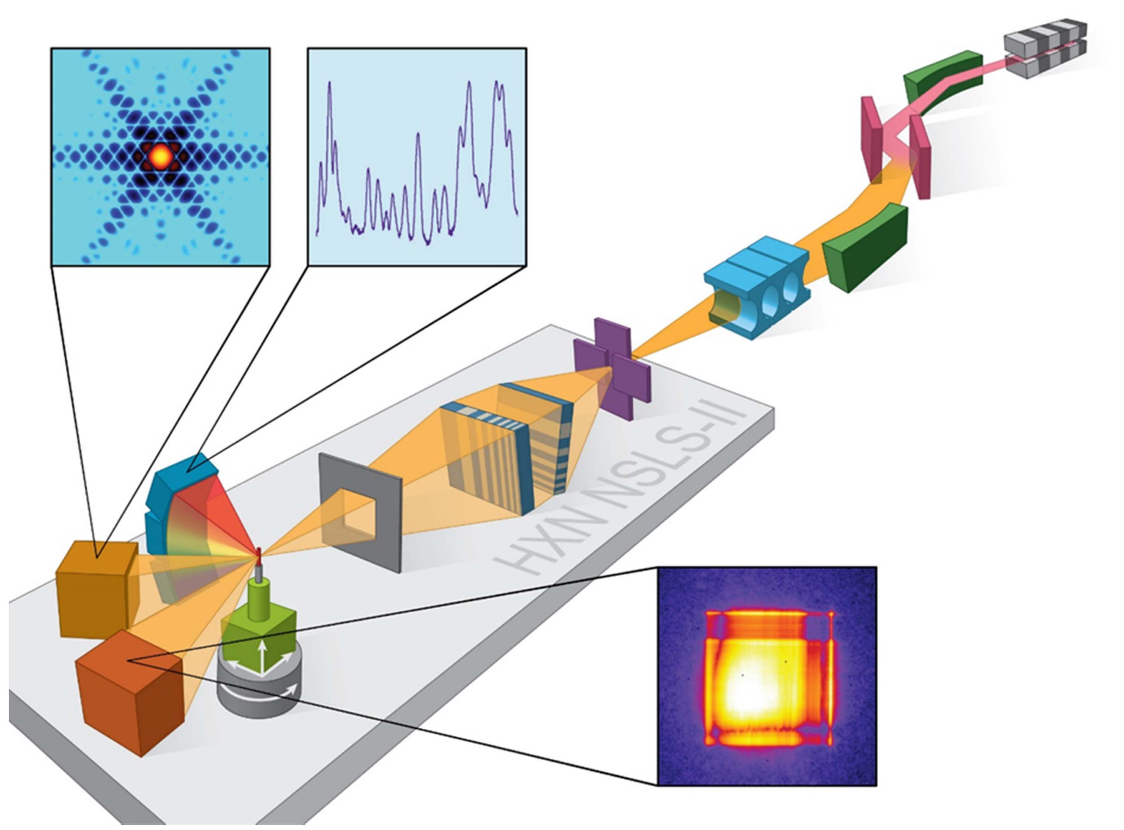

Figure 1. Schematic drawing of the HXN beamline layout. X-ray beam emitted from the undulator source goes through a collimating mirror, a double-crystal monochomator, a mirror for horizontal focusing and a set of CRLs for vertical focusing. A secondary source aperture (SSA) is used to control the coherence length of the x-ray beam in the nanofocusing optics plane. A pair of crossed MLLs focus the incident monochromatic wave into a nanobeam. An order-sorting-aperture (OSA) after MLLs is used to block undesired background and produce a clean focus. The sample is raster-scanned with respect to the nanobeam. Signals generated at each scanned position are captured by a fluorescence detector for elemental mapping, a transmission detector for absorption/phase-contrast imaging and a diffraction detector for strain analysis. The diffraction-contrast is not discussed in this work.

For imaging applications, the modulation transfer function (MTF) is of greater interest since it reveals the resolving power as a function of the spatial frequency. In the scanning fluorescence imaging, the focus intensity distribution is also the point spread function. As a result, MTF can simply be calculated from the Fourier transform of the focus intensity distribution shown in figure 2(c). In figure 2(d) we plot MTFs for both MLLs. Their intensities almost decrease linearly with frequency, indicating a relatively uniform pupil function. Note that a square pupil function results in a triangle-shape MTF [32]. If we set the frequency at which MTF drops down to 0.3 as the cut-off resolving power, we obtain a half-pitch size of 12.5 nm and 11.1 nm in horizontal and vertical directions, respectively. They are slightly smaller than FWHM sizes.

Different from ptychography reconstruction where the image resolution is not limited by the focus size, the fluorescence image quality directly depends on it. To evaluate the achieved resolution in fluorescence imaging, we performed another raster-scan on a 200 nm thick test pattern made of Pt with sufficiently small step size. Figure 3(a) is an SEM image of a test pattern with double-line structure. It was fabricated by atomic layer deposition on a deep-etched Si substrate, and have features with sizes as small as 20 nm and aspect ratios as high as 10. These fine features allow us to perform conventional knife-edge scans with strong fluorescence signals. Figures 3(b) and (c) are line scan profiles in two directions. If a perfect double-square function is assumed for the test structure, fittings to line profiles yield a FWHM focus size of $15.3 \times 16.9\ \mathrm{nm}^2$. Due to imperfections in a test structure and angular misalignment of the edge with respect to the beam, it is inevitable that this number is overestimated. Therefore we use it as the upper limit of our focus size. We also raster-scanned a more complex pattern seen in figure 3(d). The acquired x-ray fluorescence (XRF) image is displayed in figure 3(e). As evident from the comparison with SEM, fine structural variations seen in the SEM image (marked by arrows) are also captured in the fluorescence image. On the other hand, two images display systematic difference for the width of individual lines, very pronounced for example in letter 'N' and 'I'. The line-to-space ratio for the nanofabricated structure is rarely a constant throughout the entire vertical structure. Rather, it often exhibits 'over-filling' at the top, resulting in a mushroom-like feature. Consequently, the SEM image is sensitive only to the surface

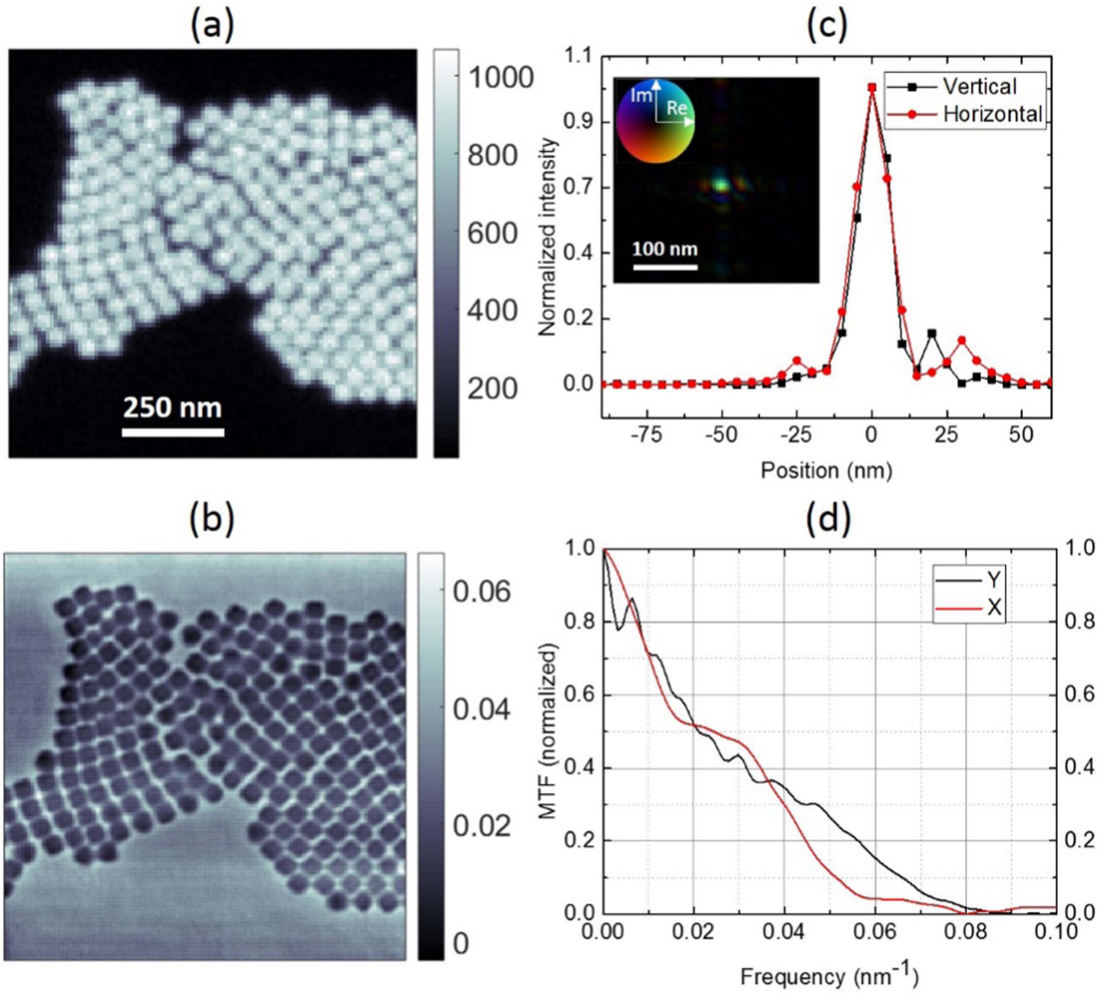

Figure 2. A fly scan with 100 × 100 pixels and 10 nm step was performed on cubic Au nanoparticles with monodispersive size of 50 nm. (a) is the acquired fluorescence image, and (b) is the reconstructed phase image of the same area using ptychography algorithm. Intensity profiles across the center of the reconstructed probe function are plotted in (c), where the inset displays the complex-valued wavefield of the probe function. (d) shows MTF functions calculated from (c).

topology, showing as if the two nearby lines are almost touching each other. In contrast, the XRF image shows that lines are narrower and better separated.

To be quantitative on the resolution, we performed a PSD analysis [33] on both SEM and XRF images (figure 3(f)). The PSD curve of the XRF image falls downs to the noise level at about the same spatial frequency in both directions. If we draw two lines to fit each PSD curve and set the interception point as the cut-off frequency, their corresponding half-pitch sizes are 10.5 nm and 10.8 nm in x and y directions, respectively. These values correspond to the spatial frequency limits of the detectable contrast, and are smallest among all characterization methods. In some sense, this analysis is equivalent to deriving the resolution from sparrow criterion, for which there is a zero contrast differential. Nevertheless, FWHM focus sizes obtained from knife-edge scan and ptychography reconstruction are within 4 nm, so are image resolutions retrieved from MTF and PSD analysis.

Efficiency is another very important metric of lens quality. The overall focusing efficiency of two MLLs was measured to be 5.7%. It was obtained by comparing the flux in the focus to that in the incoming beam. The absolute flux in the focus was estimated to be $\sim 5 \times 10^8$ photons per second at NSLS-II ring current of 150 mA. When it ramps up to the design value of 500 mA and wedged MLL [34–36] are incorporated into the scanning system, a further enhancement of the focused flux by more than 10-fold is expected.

2.3. Application for studies in material science

While the data from a test object is useful to quantify the imaging performance, the real scientific value of an x-ray microscope relies on its capability to visualize and quantify realistic samples with a non-trivial distribution of both elemental and morphological characteristics. In this work, we performed comprehensive multimodal imaging measurements to investigate the complex interfacial characteristics near the grain boundary of model ceramic systems, simultaneously collecting fluorescence, absorption, and phase images. The investigated

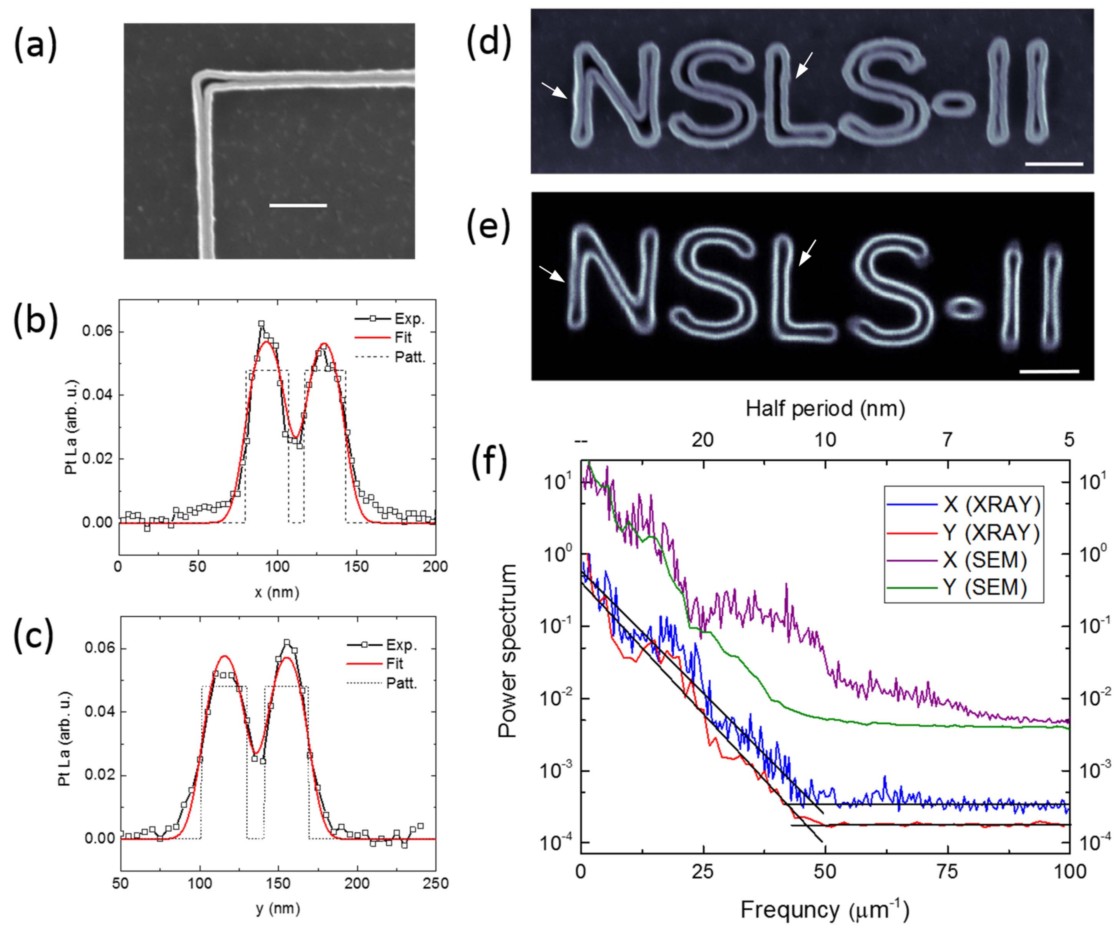

Figure 3. (a) is an SEM image of a double-line structure used for knife-edge scans. (b) and (c) are horizontal and vertical line scans across the double-line, respectively. We perform a nonlinear fitting to decouple the probe and the double-line structure represented by a double-step function (dashed black line). The fitting yields FWHM size of 15.3 nm in horizontal and 16.9 nm in vertical directions. Because the actual structure inevitably has imperfections and its edge is not as sharp as a step function, this gives an upper bound of the focus size. (d) is an SEM image of a test pattern with NSLS-II letters and (e) is the corresponding x-ray fluorescence image, which has 160 × 480 pixels with 5 nm pixel size. Subtle structural variations indicated by white arrows in (d) can be clearly seen in (e) as well. This suggests that a very high spatial resolution is achieved. (f) is a plot showing PSD analysis on both SEM and fluorescence images. For the latter, logarithmic PSD curves in horizontal and vertical directions are fitted with two lines and the interception point is defined as the cut-off frequency. The corresponding half-pitch size is the smallest detectable feature. Scale bars shown in (a), (d) and (e) are 250 nm.

material system is a mixed ionic-electronic conducting (MIEC) ceramic-based membrane, produced by sintering two precursor materials phases $Ce_{0.8}Gd_{0.2}O_{2-x}$ (CGO) and $CoFe_2O_4$ (CFO) with a volume fraction 60% CGO to 40% CFO. Exhibiting both excellent ionic and electronic conductance, this material system has important applications including energy conversion and high temperature gas separation [16–22, 37]. In particular, elemental diffusion and phase separation which lead to formation of additional material phases at grain boundary, are believed to play an important role determining the ultimate electronic and ionic transport properties of this material [38]. Through simultaneous multimodal imaging, we have unambiguously characterized the material phases at the grain boundary visualizing both elemental and morphological distributions, with unprecedented resolution and contrast. A sample of dimension, $\sim 10 \times 10 \times 1\ \mu m^3$, was harvested using a focused ion beam (FIB) from as sintered powder and mounted on a fiducialized Si substrate. Fluorescence images of Fe, Co, Gd, and Ce are displayed in figures 4(a)–(d). Pt is a foreign element that is introduced during the FIB process for sample preparation. Grains with sizes as small as ~250 nm are clearly visible, and they exhibit different chemical compositions. As evident from fluorescence images, distributions of Gd and Ce are not completely correlated, nor are distributions of Co and Fe. This indicates that a new material phase other than precursor CGO and CFO is formed at the grain boundary. Figure 4(e) is a composite map of Fe (red), Co (green), Gd (blue) and Ce (cyan). The color variation indicates a concentration ratio difference among the relevant elements. The composite map clearly displays not only the initial phases (CGO and CFO) but also a new phase with a higher Ga volume fraction, which is refereed as an emergent phase or GFCCO phase. This observation is consistent with previous electron and x-ray microscopy analysis [38, 39]. A quantitative analysis on the composition of the new material phase is out of the scope of this work and will be reported elsewhere [40].

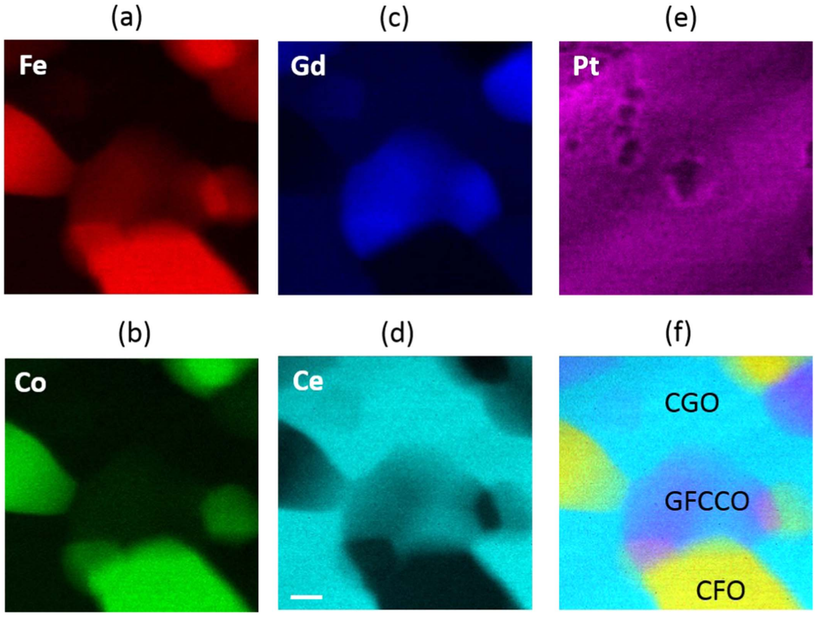

Figure 4. Distributions of (a) Fe, (b) Co, (c) Gd, (d) Ce and (e) Pt in a scanned 2 × 2 μm^2 area of the CGO-CFO membrane. The scan step is 10 nm and the scale bar is 250 nm. (f) is a composite map of overlaying Fe, Co, Gd and Ce distributions together. Each color represents a different concentration ratio among them. Three material phases, CFO, CGO and GFCC which contains all four elements can be seen. Because the x-ray beam penetrates the entire thickness, one can see some grains overlapped with each other in (f).

We also collected transmitted far-field diffraction patterns concurrently with the fluorescence signals. They are used to produce absorption- and phase-contrast images that correspond to the electron density variation. The phase image can be obtained either using a deterministic differential-phase-contrast (DPC) method [41], or iterative ptychography reconstruction. DPC is very robust and fast, but its resolution is limited by both the scan step and the probe size. In contrast, ptychography reconstruction is iterative and is computation intensive. However, the resolution of the reconstructed image is only limited by the signal to noise ratio in the far-field diffraction patterns. In addition, it decouples the probe and the object functions, thereby achieving a better contrast as well. In figures 5(a)–(c) we show the horizontal and the vertical phase-gradients and transmission amplitude obtained from the DPC algorithm. Figure 5(e) is the phase image integrated from the horizontal and vertical phase gradients. Grains with different chemical compositions can be distinguished. We observe small structural variations in figures 5(a) and (c), which are not visible in the fluorescence image. These horizontal streaks are artifacts due to a small amount of horizontal angular motion of the incidence beam (~0.1 μrad) originating from the beam conditioning optics at the time of the experiment[4].

In comparison, we show in figures 5(d) and (f) the object amplitude and the phase images obtained from the ptychography reconstruction. When compared to the DPC results (figures 5(c) and (e)), the amplitude image is no better. Similar stripe-like artifacts due to the angular beam motion are also visible. On the other hand, the reconstructed phase image exhibits significant enhancement on both resolution and contrast without displaying streak artifacts. Some of observed fine features shown in the phase image are correlated with the Pt distribution on the surface. The GFCCO phase is not well distinguished from the CGO phase due to their small difference in the electronic density. Better phase contrast could be obtained by tuning incidence x-ray energy across absorption edges of the constituent elements. We emphasize that DPC and ptychography analysis were performed on the same dataset. Depending on the preference of measurement throughput or imaging resolution, one can choose either method for phase imaging.

3. Summary

In summary, we used two crossed MLLs to achieve a FWHM focus size of 15.3 × 16.9 nm^2 based on knife-edge scans, and 13.9 × 12.3 nm^2 from ptychography reconstruction. The reconstructed focus depicted a clean central peak with low side lobes. We also showed an image resolution of 10.5 × 10.8 nm^2 (sparrow limit) from PSD analysis on the fluorescence image of a test pattern, which is very close to a size of 12.5 × 11.1 nm^2 based on

---

[4] A feedback system has been implemented to improve the beam stability afterward and since then streak artifacts in images have disappeared.

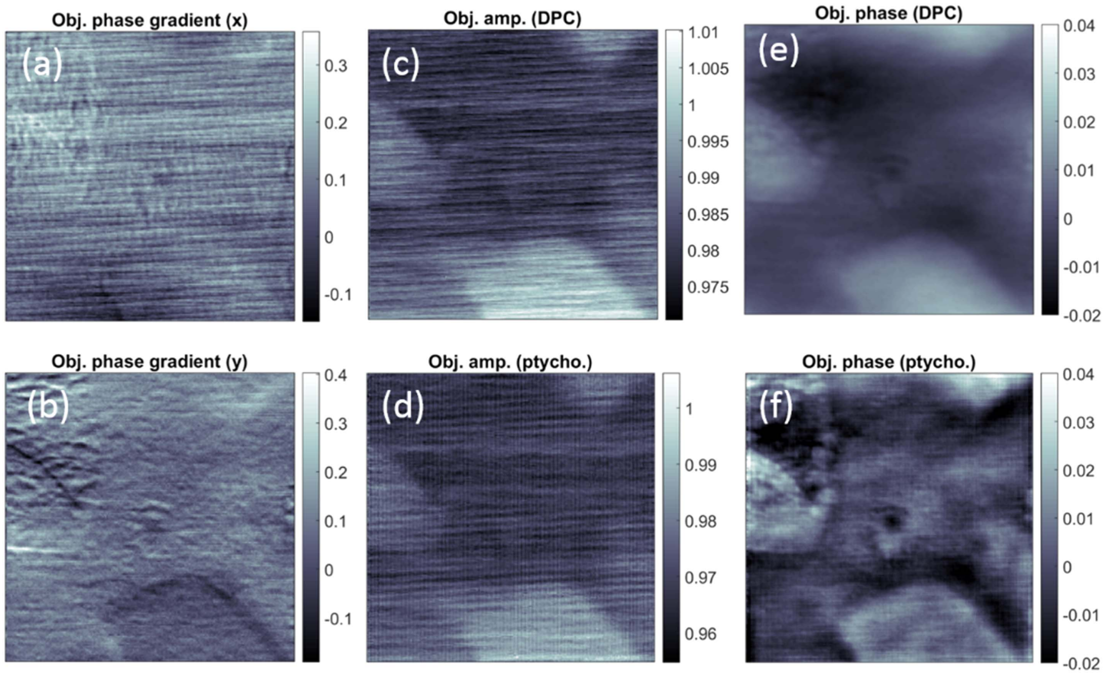

Figure 5. In the same raster-scan for fluorescence (figure 3), farfield images are collected concurrently to produce phase-gradient images in horizontal (a) and vertical (b) directions, transmission amplitude (c) and the integrated phase (e) images. They are all obtained from the DPC algorithm. (d) and (f) are the reconstructed amplitude and phase obtained from the ptychography algorithm, using the same dataset. Stripes seen in (a), (c) and (d) are due to beam instability in the horizontal direction.

MTF functions. The lens system has an overall efficiency of 5.7% at 12 keV. At the ring current of 150 mA at NSLS-II, this corresponds to a flux in the focus of $\sim 5 \times 10^8$ photon per second. We demonstrated that nano-Mii at HXN beamline of NSLS-II, with a nearly 10 nm resolution provided by MLL optics, is capable of performing routine multimodal x-ray imaging on a real sample that has complicated structural and elemental variations. Our work is a manifestation of an important milestone achieved in the field of hard x-ray scanning microscopy, since it eliminates the gap between demonstration of optical resolution under ideal experimental conditions and actual imaging resolution for routine scientific measurements.

Acknowledgment

HY thanks Fang Lu and Ming Lu for supplying test objects. This research used resources of the Hard X-ray Nanoprobe Beamline of the National Synchrotron Light Source II, a US Department of Energy (DOE) Office of Science User Facility operated for the DOE Office of Science by Brookhaven National Laboratory under Contract No. DE-SC0012704. APC, WKSC, and KSB acknowledge financial support from an Energy Frontier Research Center on Science Based Nano-Structure Design and Synthesis of Heterogeneous Functional Materials for Energy Systems (HeteroFoaM Center) funded by the US Department of Energy, Office of Science, Office of Basic Energy Sciences (Award no. DE-SC0001061).

ORCID iDs

Hanfei Yan https://orcid.org/0000-0001-6824-0367
Xiaojing Huang https://orcid.org/0000-0001-6034-5893
Kyle S Brinkman https://orcid.org/0000-0002-2219-1253

References

[1] Hruszkewycz S O, Holt M V, Murray C E, Bruley J, Holt J, Tripathi A, Shpyrko O G, McNulty I, Highland M J and Fuoss P H 2012 Quantitative nanoscale imaging of lattice distortions in epitaxial semiconductor heterostructures using nanofocused x-ray Bragg projection ptychography *Nano Lett.* **12** 5148

[2] Thibault P, Dierolf M, Menzel A, Bunk O, David C and Pfeiffer F 2008 High-resolution scanning x-ray diffraction microscopy *Science* **321** 379

[3] Ice G E, Budai J D and Pang J W L 2011 The race to x-ray microbeam and nanobeam science *Science* **334** 1234

[4] Sakdinawat A and Attwood D 2010 Nanoscale x-ray imaging *Nat. Photon.* **4** 840
[5] Vogt U, Parfeniukas K, Stankevič T, Kalbfleisch S, Liebi M, Matej Z, Björling A, Carbone G, Mikkelsen A and Johansson U 2017 First x-ray nanoimaging experiments at NanoMAX *SPIE* **10389** 103890K
[6] Silva J C D, Pacureanu A, Yang Y, Fus F, Hubert M, Bloch L, Salome M, Bohic S and Cloetens P 2017 High-energy cryo x-ray nano-imaging at the ID16A beamline of ESRF *SPIE* **10389** p 103890F
[7] Schroer C G 2016 Hard x-ray nanoprobe of Beamline P06 at PETRA III *AIP Conf. Proc.* **1741** 030007
[8] Suzuki M *et al* 2013 A hard x-ray nanospectroscopy station at SPring-8 BL39XU *J. Phys.: Conf. Ser.* **430** 012017
[9] Winarski R P *et al* 2012 A hard x-ray nanoprobe beamline for nanoscale microscopy *J. Synchrotron Radiat.* **19** 1056
[10] http://diamond.ac.uk/Beamlines/Spectroscopy/I14.html
[11] Mohacsi I, Vartiainen I, Rosner B, Guizar-Sicairos M, Guzenko V A, McNulty I, Winarski R, Holt M V and David C 2017 Interlaced zone plate optics for hard x-ray imaging in the 10 nm range *Sci. Rep.* **7** 43624
[12] Huang X *et al* 2013 11 nm hard x-ray focus from a large-aperture multilayer Laue lens *Sci. Rep.* **3** 3562
[13] Mimura H *et al* 2010 Breaking the 10 nm barrier in hard-x-ray focusing *Nat. Phys.* **6** 122
[14] Da Silva J C, Pacureanu A, Yang Y, Bohic S, Morawe C, Barrett R and Cloetens P 2017 Efficient concentration of high-energy x-rays for diffraction-limited imaging resolution *Optica* **4** 492
[15] Yan H, Conley R, Bouet N and Chu Y S 2014 Hard x-ray nanofocusing by multilayer Laue lenses *J. Phys. D: Appl. Phys.* **47** 263001
[16] Shao Y Y, Ding F, Xiao J, Zhang J, Xu W, Park S, Zhang J G, Wang Y and Liu J 2013 Making Li-air batteries rechargeable: material challenges *Adv. Funct. Mater.* **23** 987
[17] Brinkman K, Iijima T and Takamura H 2010 The oxygen permeation characteristics of $Bi_{1-x}Sr_xFeO_3$ mixed ionic and electronic conducting ceramics *Solid State Ion.* **181** 53
[18] Takamura H, Ogawa M, Suehiro K, Takahashi H and Okada M 2008 Fabrication and characteristics of planar-type methane reformer using ceria-based oxygen permeable membrane *Solid State Ion.* **179** 1354
[19] Sunarso J, Baumann S, Serra J M, Meulenberg W A, Liu S, Lin Y S and da Costa J C D 2008 Mixed ionic-electronic conducting (MIEC) ceramic-based membranes for oxygen separation *J. Membr. Sci.* **320** 13
[20] Kagomiya I, Iijima T, Kakuta H and Takamura H 2005 Oxygen permeable $Ce_{0.8}Gd_{0.2}O_{1.9}$–$CoFe_2O_4$ thin films prepared on porous $Ce_{0.8}Gd_{0.2}O_{1.9}$ substrates *Electrochem. Solid State Lett.* **8** A70
[21] Bouwmeester H J M 2003 Dense ceramic membranes for methane conversion *Catal. Today* **82** 141
[22] Dyer P N, Richards R E, Russek S L and Taylor D M 2000 Ion transport membrane technology for oxygen separation and syngas production *Solid State Ion.* **134** 21
[23] Nazaretski E, Yan H, Lauer K, Bouet N, Huang X, Xu W, Zhou J, Shu D, Hwu Y and Chu Y S 2017 Design and performance of an x-ray scanning microscope at the hard x-ray nanoprobe beamline of NSLS-II *J. Synchrotron Radiat.* **24** 1113
[24] Yan H *et al* 2011 Two dimensional hard x-ray nanofocusing with crossed multilayer Laue lenses *Opt. Express* **19** 15069
[25] Nazaretski E *et al* 2015 Pushing the limits: an instrument for hard x-ray imaging below 20 nm *J. Synchrotron Radiat.* **22** 336
[26] Yan H, Huang X, Bouet N, Zhou J, Nazaretski E and Chu Y S 2017 Achieving diffraction-limited nanometer-scale x-ray point focus with two crossed multilayer Laue lenses: alignment challenges *Opt. Express* **25** 25234
[27] Huang X J, Lauer K, Clark J N, Xu W H, Nazaretski E, Harder R, Robinson I K and Chu Y S 2015 Fly-scan ptychography *Sci. Rep.* **5** 9074
[28] Deng J J, Nashed Y S G, Chen S, Phillips N W, Peterka T, Ross R, Vogt S, Jacobsen C and Vine D J 2015 Continuous motion scan ptychography: characterization for increased speed in coherent x-ray imaging *Opt. Express* **23** 5438
[29] Pelz P M, Guizar-Sicairos M, Thibault P, Johnson I, Holler M and Menzel A 2014 On-the-fly scans for x-ray ptychography *Appl. Phys. Lett.* **105** 251101
[30] Clark J N, Huang X J, Harder R J and Robinson I K 2014 Continuous scanning mode for ptychography *Opt. Lett.* **39** 6066
[31] Huang X J, Yan H F, Ge M Y, Ozturk H, Nazaretski E, Robinson I K and Chu Y S 2017 Artifact mitigation of ptychography integrated with on-the-fly scanning probe microscopy *Appl. Phys. Lett.* **111** 5
[32] Goodman J W 2005 *Introduction to Fourier Optics* (Greenwood Village, CO: Roberts & Company Publishers)
[33] Chen T Y, Chen Y T, Wang C L, Kempson I M, Lee W K, Chu Y S, Hwu Y and Margaritondo G 2011 Full-field microimaging with 8 keV x-rays achieves a spatial resolutions better than 20 nm *Opt. Express* **19** 19919
[34] Morgan A J *et al* 2015 High numerical aperture multilayer Laue lenses *Sci. Rep.* **5** 09892
[35] Huang X *et al* 2015 Achieving hard x-ray nanofocusing using a wedged multilayer Laue lens *Opt. Express* **23** 12496
[36] Yan H F, Maser J, Macrander A, Shen Q, Vogt S, Stephenson G B and Kang H C 2007 Takagi-Taupin description of x-ray dynamical diffraction from diffractive optics with large numerical aperture *Phys. Rev.* B **76** 115438
[37] Brinkman K and Huang K 2016 Solid oxide fuel cells and membranes *Chem. Eng. Prog.* **112** 44–9
[38] Harris W M *et al* 2014 Characterization of 3D interconnected microstructural network in mixed ionic and electronic conducting ceramic composites *Nanoscale* **6** 4480
[39] Lin Y, Fang S M, Su D, Brinkman K S and Chen F L 2015 Enhancing grain boundary ionic conductivity in mixed ionic-electronic conductors *Nat. Commun.* **6** 6824
[40] Ge M, Huang X, Yan H, Li L, Nazaretski E, Chiu W K S, Xin H and Chu Y S 3D quantitative analysis of chemical composition by scanning x-ray nanoprobe through self-absorption correction in preparation
[41] Yan H, Chu Y S, Maser J, Nazaretski E, Kim J, Kang H C, Lombardo J J and Chiu W K S 2013 Quantitative x-ray phase imaging at the nanoscale by multilayer Laue lenses *Sci. Rep.* **3** 1307